

On the excitation of the infrared knots in the HH99 outflow [★]

C. M^cCoey^{1†}, T. Giannini², D.R. Flower¹, A. Caratti o Garatti^{2,3}

¹ *Physics Department, The University, Durham DH1 3LE, UK*

² *INAF-Osservatorio Astronomico di Roma, via Frascati 33, I-00040 Monteporzio Catone, Italy*

³ *Università degli Studi 'Tor Vergata', via della Ricerca Scientifica 1, I-00133 Roma, Italy*

Received date; Accepted date

ABSTRACT

We present near infrared (IR) spectra (0.98–2.5 μm) from the group of Herbig-Haro (HH) objects comprising HH99: a series of knots forming a bow, HH99B, and a separate knot, HH99A. Observations of H₂, [Fe II] and [C I] are used to constrain shock model parameters and determine the origin of the emission. Previous work has shown that it is likely that the atomic and ionic emission arises in regions of higher ionization than the molecular emission. On the basis of observations, it has often been suggested that the [Fe II] and [C I] emission could arise, for example, at the apex of a bow shock, with the H₂ emission produced in the wings. Accordingly, we have combined models of C-component and J-type shocks in order to reproduce the observed H₂, [Fe II] and [C I] line spectra. We can account for the H₂ emission towards the HH99B complex by means of J-type shocks with magnetic precursors. We derive shock velocities of about 30 km s^{−1} and ages of order 100 yr; the pre-shock gas has a density $n_{\text{H}} \approx 10^4 \text{ cm}^{-3}$ and the magnetic field $B \approx 100 \mu\text{G}$. The J-type shocks required to reproduce the intensities of the observed [Fe II] and [C I] lines have velocities of 50 km s^{−1}. It is necessary to assume that Fe has been previously eroded from grains, probably by the earlier passage of a C-type shock wave. Thus, our analysis supports the view that molecular outflows are episodic phenomena whose observed emission arises in shock waves.

Key words: stars: circumstellar matter – Infrared: ISM – ISM: Herbig-Haro objects – ISM: jets and outflows – shock waves

1 INTRODUCTION

Bipolar outflows are produced during the accretion phase of low mass star formation in molecular clouds. The large scale outflows are observed in the infrared domain and are traced, for example, by rotational transitions of CO (e.g. $J = 3 \rightarrow 2$, $J = 2 \rightarrow 1$). The outflows often terminate in a bow-shaped structure and are marked by chains of Herbig-Haro objects, which are condensations of warm gas observable in the visible and in the near infrared. It is commonly thought that HH objects are produced in episodic events and are: dense regions of the ambient interstellar medium (ISM) which have been shocked by the passage of the outflow; or ejecta from the forming star or its accretion disk; or the consequence of instabilities within the outflow. The observed molecular line shifts and widths and the presence of

refractory species, such as Fe and Si, with abundances higher than in the ambient medium, are indicative of shock waves. HH outflows have dynamical lifetimes of the order of 10^3 – 10^5 years (Bachiller, 1996), whereas the timescale for a shock wave to attain steady state can be of the order of 10^5 years (Pineau des Forêts, Flower & Chièze, 1997; Chièze, Pineau des Forêts & Flower, 1998). It follows that non-equilibrium shock modelling may be required when simulating the observed line intensities.

Shock waves are usually classified as ‘jump’ (‘J-type’) or continuous (‘C-type’) (see Draine, 1980). Each type of shock wave gives rise to different excitation conditions in the gas. In a J-type shock of velocity 40 km s^{−1}, the temperature immediately behind the discontinuity approaches 10^5 K, as compared with $T \approx 10$ K in the preshock gas (see Figure 1). The gas density increases by no more than a factor of 4 at the discontinuity, but the gas continues to be compressed in the cooling flow. C-type shocks occur in regions of low ionization, where the strength of the coupling between the charged and neutral fluids is insufficient to prevent a velocity

[★] Based on observations collected at the European Southern Observatory, Paranal, Chile (70.C-138)

[†] E-mail: carolyn.mccoey@durham.ac.uk

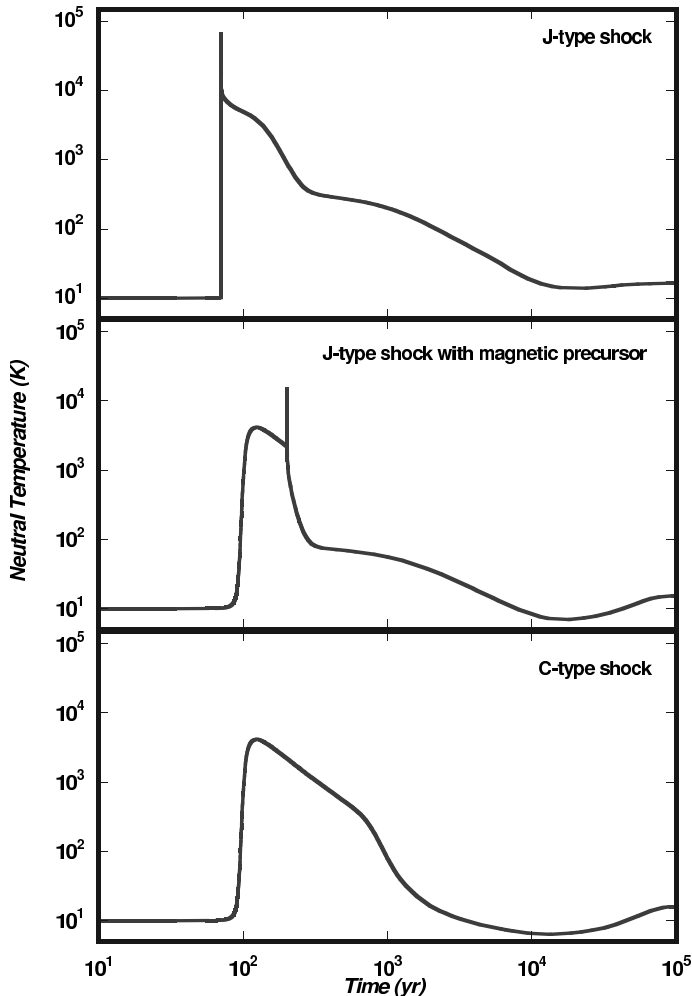


Figure 1. Temperature profiles of J-type (top panel), J-type with magnetic precursor (middle panel) and C-type (bottom panel) shock waves ($v_s=40$ km s $^{-1}$, $n_H=10^4$ cm $^{-3}$, $B=100$ μ G). In evolutionary terms, a J-type shock with a magnetic precursor can be considered to be intermediate between J-type and C-type shocks. Note the increase in shock width and decrease in peak temperature in the evolution from a J- to a C-type shock.

difference developing between the two fluids. The charged fluid and the magnetic field are compressed ahead of the neutral fluid; this results in a broadening of the shock wave and a decrease in the peak temperature (see Figure 1). In the presence of a sufficiently strong magnetic field, an initially J-type shock may evolve into C-type. At early times, a J-type discontinuity remains embedded in the C-type flow (Pineau des Forêts, Flower & Chièze, 1997; Smith & Mac Low, 1997; Chièze, Pineau des Forêts & Flower, 1998; Lesaffre, Chièze, Cabrit & Pineau des Forêts, 2004a,b). These ‘intermediate’ types of shock wave are referred to as ‘J-type with a magnetic precursor’; they are narrower than the equivalent steady-state C-type shock waves and have higher maximum temperatures.

The large number of IR rovibrational emission lines of H $_2$ observed towards HH objects suggests the importance of H $_2$ as a coolant. The excitation diagrams derived from these lines can be used to constrain the model parameters, such as the shock velocity and age, and the pre-shock gas

density. Comparison of the observed H $_2$ emission with the predictions of shock models has shown the best agreement for shock waves which are C-type or have a C-component, i.e. J-type with a magnetic precursor (Giannini et al., 2004; Flower et al., 2003; Le Bourlot et al., 2002).

In addition to being observable in rovibrational transitions of H $_2$, HH outflows can be traced through their emission in high- J CO and other molecular lines and the emission of atoms and ions (e.g. Liseau, Ceccarelli & Larsson, 1996; Benedettini et al., 2000). With increasing shock speed, the temperature and density of the gas in the shock wave increase; H $_2$ is dissociated and H begins to be ionized. As a consequence, the contribution of H $_2$ to the radiative cooling decreases and that of other species, such as H $_2$ O, CO, O, C and Fe $^{+}$, assumes greater importance. The strongest ionic and atomic lines observed are those of [Fe II] and [C I]. In a C-type shock wave, or in a magnetic precursor to a J-type shock, charged grains can be eroded by neutral particles, owing to the relative streaming of the charged and neutral fluids. At sufficiently high shock speeds, the (refractory) grain cores can be partially eroded, releasing elements such as Fe and C into the gas phase; see May et al. (2000). Neutral iron is ionized rapidly in the gas phase, predominantly through charge transfer reactions with ions, such as H $_3^{+}$ and H $_3$ O $^{+}$, which have larger ionization potentials. Fe $^{+}$ may then be excited collisionally and emit the [Fe II] forbidden line spectrum.

Giannini et al. (2004) showed that it is not possible to reproduce the atomic and ionic emission observed in HH objects with the same planar model as is deduced from the H $_2$ emission; the atomic and ionic emission requires a higher degree of ionization. Several possible explanations have been proposed for the presence of ionized species, such as [Fe II], in conjunction with H $_2$. For example, Gredel (1994, 1996) suggested curved J-type shocks, while other authors have proposed a combination of C- and J-type shocks (Molinari et al., 2000) or J-type shocks with magnetic precursors (Hartigan, Curiel & Raymond, 1989). Some observed features of HH objects, such as the line widths and range of excitation conditions inferred from H $_2$ observations (e.g. Eislöffel, Smith & Davis, 2000) and the existence of ‘caps’ of [Fe II] emission ahead of that of H $_2$ (e.g. Davis, Smith & Eislöffel, 2000), have led to suggestions that the H $_2$ emission arises in the wings and atomic and ionic emission originates at the apex of a bow shock. Alternatively, the atomic and ionic emission might arise in a reverse shock, in the jet, and the H $_2$ emission in the molecular gas which has been impacted by the jet. In either case, the degree of ionization must be sufficient for electron collisions to dominate the excitation of the atomic and ionic emission lines; such conditions can be realized in J-type shocks.

We identified as a good observational case to test shock models the HH99 region ($\alpha = 19^h02^m05.4^s$, $\delta = -36^\circ54'40''$ (J2000.0)), a Herbig-Haro complex in the RCrA molecular core ($d = 130$ pc: Marraco & Rydgren, 1981). This complex comprises a prototype of bow shock (namely HH99B) and a bright wing feature (knot A), probably originating in the interaction of the flow with a dense ambient clump or cloudlet (Davis et al., 1999). On the basis of optical images and high resolution spectra, Hartigan & Graham (1987) have suggested that the HH99 complex is the redshifted lobe of the HH100 flow, powered by the embedded protostar HH100

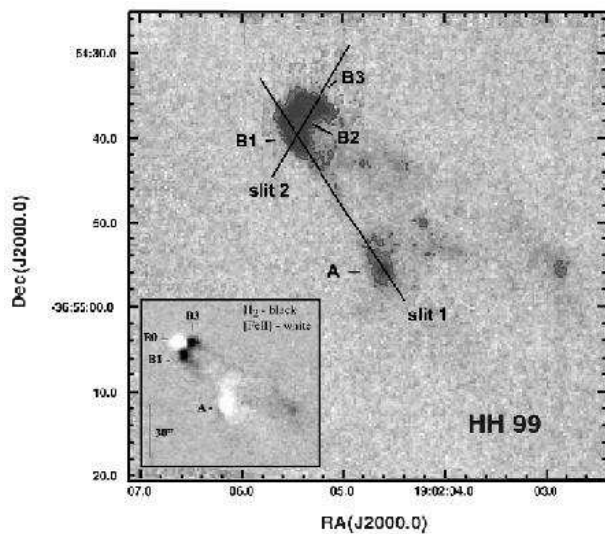


Figure 2. HH99: H₂ (2.122 μ m) image (continuum not subtracted) obtained at ESO-NTT with Sofi IR camera. Knot labels and slit positions are superposed. The inset shows Figure 1b of Davis et al. (1999), on which we have also marked the knot B0.

IR. More recently, near infrared images have demonstrated that the bow shock/jet define a direction consistent with the position of the infrared source IRS 9 and the pre-main sequence star RCrA (Wilking et al., 1997). The low resolution K-spectrum of HH99B3 and echelle spectra of the H₂ 2.122 μ m line have been obtained by Davis et al. (1999).

In order to better probe the temperature along the shocked gas and to constrain observationally the shock model parameters, we have investigated spectroscopically the HH99 complex by observing the complete (0.98 – 2.5 μ m) near infrared spectrum across the bow and along the wing (see Figure 2). We present the observations of HH99 in Section 2 and discuss the model predictions in Section 3, where we also give a brief description of the shock code which was used. We summarize our findings in Section 4.

2 OBSERVATIONS AND DATA REDUCTION

The spectroscopic observations of HH99 were made in July 2002, at the ESO-VLT, with the ISAAC near infrared camera and at a resolution of 0.147''/pixel (Cuby et al., 2003). In order to investigate the head and wings of the bow shock, long-slit spectra were obtained for two different position angles (P.A. = 32.4° and 329.5°, referred to as slit 1 and slit 2 respectively; see Figure 2) in four segments, centered on the bands *z*, *J*, *H* and *K*, covering a spectral range from 0.98 to 2.50 μ m. With reference to the nomenclature adopted by Davis et al. (1999), slit 1 encompasses knots A, B1 and a further zone of [Fe II] emission, visible in their Figure 1, to which we shall refer as B0. Slit 2 encompasses knots B1, B2 and B3. The slit width was 0.6'', corresponding to a spectral resolution from about 750 to 900, moving from the shorter to the longer wavelengths. To perform our spectroscopic measurements, we adopted the usual ABB'A' configuration, for a total integration time of 400 s per band. All the raw data

were reduced by using the IRAF¹ package, applying standard procedures for sky subtraction, flat-fielding and bad pixel removal. Observations were sky subtracted and corrected for the curvature, due to optical distortions, by fitting sky lines row-by-row. Atmospheric features were removed by dividing the spectra by a telluric standard star (O spectral type), normalized to the blackbody function at the star's temperature and corrected for hydrogen recombination absorption features intrinsic to the star. The wavelength calibration was obtained using sky OH lines (Rousselot et al., 2000).

All the observed spectra are rich both in H₂ (vibrational quantum number $1 \leq v \leq 4$) and ionic lines, as observed in other HH objects (Nisini et al., 2002). Figure 3 shows the spectrum of the knot B0, where the most prominent ionic features are detected, mainly [Fe II] lines emitted by the first 13 energy levels. The other ionic features detected in this knot are the [C I] doublet at 0.983 and 0.985 μ m and, at a lower S/N, the [S II] 1.029, 1.032 and 1.034 μ m transitions, two [N I] blended doublets (1.040/1.041 μ m) and the He I 1.083 μ m recombination line. Pa β is also just visible at S/N ≤ 3 .

The spectra of the other knots observed present H₂ (for $v \leq 3$), [C I] and [Fe II] transitions, but other ionic features are weak or absent, probably indicating lower excitation conditions along the bow wings.

Line fluxes have been obtained by fitting the line profile with a single or, in the case of blending, a double gaussian. Flux calibration (associated uncertainty: 10%) was achieved by observing the photometric standard star HR7136 in the *J*, *H* and *K* bands; the photometric data were taken from the catalogue of Van der Blik et al. (1996). Ratios of lines falling in different bands have an uncertainty of about 15%, due mainly to seeing variations during the night; this error was estimated by measuring the intensities of lines present in two adjacent bands.

The complete list of the line fluxes is available only in the electronic version of this paper. In Tables 1 and 2, we report, as examples, the lines identified in the B0 spectrum (column 1), together with the vacuum wavelengths (column 2) and the measured fluxes (column 3). The uncertainties associated with these data derive only from the rms of the local baseline, multiplied by the linewidths (which are always comparable with the width of the instrumental profile). Our line fluxes are systematically lower than indicated by the photometry of Davis et al. (1999). We believe that these discrepancies are attributable to the fact that the areas of emission covered by our slits are from three to ten times smaller than the dimensions of the knots. However, the lines fluxes measured in knot B3 are in good agreement with those derived from low resolution spectroscopy by Davis et al. (1999), if the different slit widths and orientations are taken into account.

The use of ratios of intensities of pairs of lines emitted by a common upper level has long been recognized as an important tool for deriving extinction in HH objects (see,

¹ IRAF (Image Reduction and Analysis Facility) is distributed by the National Optical Astronomy Observatories, which are operated by AURA, Inc., under a cooperative agreement with the National Science Foundation.

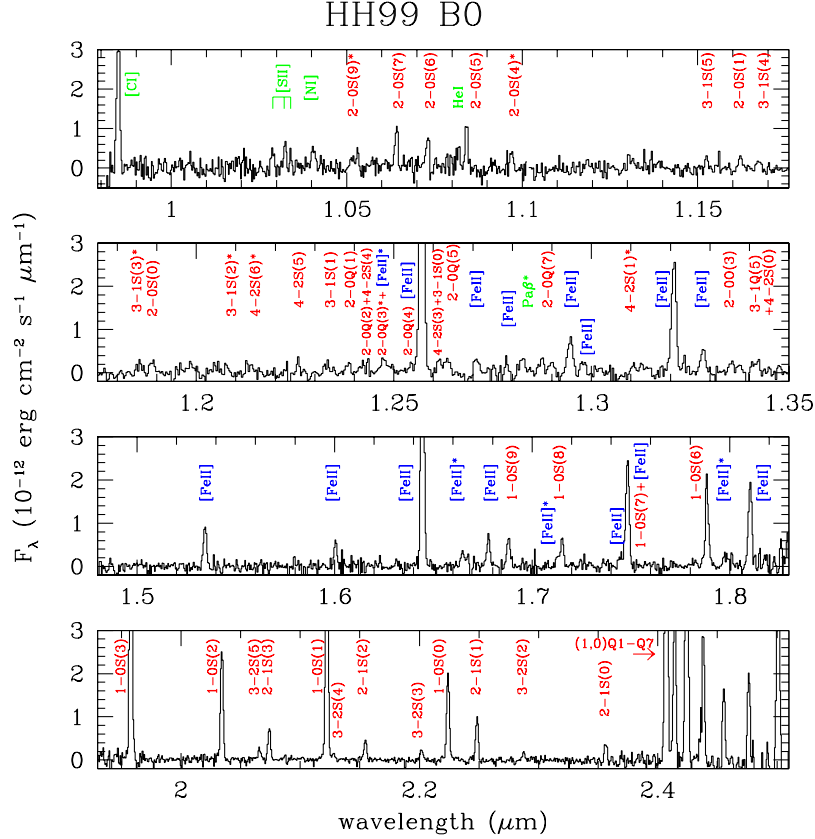


Figure 3. 0.95–2.5 μm low resolution spectrum of knot B0 in HH99. An asterisk near the line identification marks detections between 2 and 3 σ .

for example, Gredel 1994). In the spectra of HH99 knots, lines fulfilling this criterion come both from [Fe II] and H₂, and this circumstance enables to make two independent determinations of the visual extinction, A_V . From the ratio of the intensities of the 1.257 μm and 1.644 μm lines, which are the [Fe II] lines observed with the highest signal-to-noise ratio, we derive $4 \leq A_V \leq 10$ mag (see Table 4), when the reddening law of Rieke & Lebofsky (1985) is adopted. Values of A_V which are systematically lower, by about 2 to 3 mag, are obtained when using pairs of H₂ transitions [such as 2-0 S(i)/2-0 Q(i+2) and 3-1 S(i)/3-2 S(i)]. This result, which has been found in other Herbig-Haro condensations (e.g. Giannini et al. 2004, Nisini et al. 2002), shows that the iron lines arise in regions which are more deeply embedded than those responsible for the molecular hydrogen emission.

3 COMPARISON WITH PREDICTIONS OF SHOCK MODELS

In this Section, we compare the predictions of the shock models with the H₂, [Fe II] and [C I] emission observed towards HH99. Relevant aspects of the modelling of the emission are summarized in Section 3.1, and the results are presented and discussed in Section 3.2.

3.1 The model

3.1.1 Theory

The features of the shock model are described by Le Bourlot et al. (2002) and Flower et al. (2003). Here, we review only those aspects relevant to the present study. The code, MHD_VODE, solves for one-dimensional, planar, multi-fluid flow and can simulate not only steady state J- and C-type shock waves, but also non-equilibrium J-type shocks with magnetic precursors. The differential equations which determine the abundances of the chemical species are solved in parallel with the magnetohydrodynamical conservation equations for the neutral, positively and negatively charged fluids. The chemical network consisted of over 1000 reactions involving 138 species.

The method used to calculate the emission by molecular hydrogen was explained by Giannini et al. (2004). The processes which populate and depopulate the rovibrational levels of H₂ are: collisional excitation and de-excitation; spontaneous radiative decay; collisional dissociation and ionization; and reformation of H₂ on grains, which occurs in the wake of the shock wave. We calculate the distribution of population among 150 rovibrational levels of H₂ (i.e. up to an energy of 3.9×10^4 K). The equations for the level populations are solved in parallel with the chemical and dynamical conservation equations. This approach is essential to ensure the

Table 1. H₂ lines observed in HH99B0.

Term	λ (μm)	$F \pm \Delta F$ ($10^{-16} \text{erg cm}^{-2} \text{s}^{-1}$)
2-0 S(9)	1.053	4.9 ± 2.0^a
2-0 S(7)	1.064	13.4 ± 2.7
2-0 S(6)	1.073	7.4 ± 1.9
2-0 S(5)	1.085	17.6 ± 2.3
2-0 S(4)	1.100	9.1 ± 4.0^a
3-1 S(5)	1.152	6.4 ± 1.3
2-0 S(1)	1.162	5.6 ± 1.2
3-1 S(4)	1.167	3.7 ± 1.2
3-1 S(3)	1.186	5.4 ± 2.0^a
2-0 S(0)	1.189	3.6 ± 1.1
3-1 S(2)	1.207	3.4 ± 1.4^a
4-2 S(6)	1.214	3.2 ± 1.2^a
4-2 S(5)	1.226	3.9 ± 1.2
3-1 S(1)	1.233	5.7 ± 0.7
2-0 Q(1)	1.238	4.6 ± 1.0
2-0 Q(2)+4-2S(4)	1.242+1.242	3.6 ± 0.8
2-0 Q(3)+ [Fe II] $a^4D_{3/2} - a^6D_{5/2}$	1.247+1.248	4.0 ± 1.4^a
2-0 Q(4)	1.254	2.9 ± 0.6
4-2 S(3)+3-1S(0)	1.261+1.262	6.7 ± 1.2
2-0 Q(5)	1.263	5.2 ± 1.7
2-0 Q(7)	1.287	5.2 ± 0.9
4-2 S(1)	1.311	5.0 ± 1.8^a
2-0 O(3)	1.335	5.7 ± 1.3
3-1 Q(5)+4-2S(0)	1.342+1.342	5.9 ± 1.2
1-0 S(9)	1.688	14.2 ± 2.0
1-0 S(8)	1.715	12.1 ± 1.8
1-0 S(7)+ [Fe II] $a^4P_{3/2} - a^4D_{7/2}$	1.748+1.749	47.5 ± 1.4
1-0 S(6)	1.788	34.6 ± 1.3
1-0 S(3)	1.958	199.6 ± 6.5
1-0 S(2)	2.034	61.0 ± 1.8
3-2 S(5)	2.066	7.2 ± 1.4
2-1 S(3)	2.073	18.3 ± 1.4
1-0 S(1)	2.122	147.4 ± 1.4
3-2 S(4)	2.127	4.5 ± 0.7
2-1 S(2)	2.154	13.1 ± 1.4
3-2 S(3)	2.201	8.5 ± 1.4
1-0 S(0)	2.223	48.8 ± 1.1
2-1 S(1)	2.248	26.6 ± 1.2
3-2 S(2)	2.287	7.0 ± 1.2
2-1 S(0)	2.355	14.2 ± 1.3
1-0 Q(1)	2.407	212.4 ± 4.3
1-0 Q(2)	2.413	84.7 ± 4.3
1-0 Q(3)	2.424	209.5 ± 4.3
1-0 Q(4)	2.437	67.1 ± 4.1
1-0 Q(5)	2.455	54.5 ± 4.9
1-0 Q(6)	2.476	48.9 ± 11.7
1-0 Q(7)	2.500	140.8 ± 15.0

Notes: ^aS/N between 2 and 3.

accuracy of the computed H₂ column densities, because the level populations do not respond instantaneously to changes in the physical state of the gas. Radiative pumping of H₂ is considered to be unimportant compared with collisional excitation within a shock wave (see Giannini et al., 2004) and is not taken into account.

The H₂ emission line intensities predicted by the shock model can be used to generate an excitation diagram (also known as a Boltzmann plot); this is a plot of $\ln(N_{vJ}/g_J)$ against E_{vJ}/k , where N_{vJ} (cm⁻²) is the column density of level (v, J) , E_{vJ}/k (K) is its excitation energy, and $g_J =$

$(2J+1)(2I+1)$ is its statistical weight. The nuclear spin quantum number $I = 1$ for ortho-H₂ and $I = 0$ for para-H₂. Under conditions of thermodynamic equilibrium, this plot is a straight line whose gradient is inversely proportional to the kinetic temperature of the gas. In a shock wave, on the other hand, there is a range of kinetic temperatures. If the gas is in local thermodynamic equilibrium (LTE), the Boltzmann plot is a smooth curve, with little scatter of the points about the median line. Departures from LTE enhance the scatter. Thus, the excitation diagram is a useful diagnostic tool when studying H₂ emission lines from shocked molecular gas.

Table 2. Atomic and Ionic lines observed in HH99B0.

Term	λ (μm)	$F \pm \Delta F$ ($10^{-16} \text{erg cm}^{-2} \text{s}^{-1}$)
[C I] $^1D_2 - ^3P_1 +$ [C I] $^1D_2 - ^3P_2$	0.983+0.985	66.1 ± 5.6
[S II] $^2P_{3/2} - ^2D_{3/2}$	1.029	10.3 ± 1.7
[S II] $^2P_{3/2} - ^2D_{5/2}$	1.032	9.5 ± 1.2
[S II] $^2P_{3/2} - ^2D_{3/2}$	1.034	5.6 ± 1.0
[N I] $^2P_{3/2,1/2} - ^2D_{5/2} + ^2P_{3/2,1/2} - ^2D_{3/2}$	1.040-1.041	11.4 ± 2.2
He I $^3S_1 - ^3P_{0,1,2}^o$	1.083	7.9 ± 2.1
[Fe II] $a^4D_{7/2} - a^6D_{9/2}$	1.257	119.1 ± 1.0
[Fe II] $a^4D_{1/2} - a^6D_{1/2}$	1.271	8.1 ± 1.7
[Fe II] $a^4D_{3/2} - a^6D_{3/2}$	1.279	10.5 ± 2.9
Pa β	1.282	4.8 ± 2.0^a
[Fe II] $a^4D_{5/2} - a^6D_{5/2}$	1.295	16.6 ± 1.8
[Fe II] $a^4D_{3/2} - a^6D_{1/2}$	1.298	4.7 ± 1.0
[Fe II] $a^4D_{7/2} - a^6D_{7/2}$	1.321	41.0 ± 1.8
[Fe II] $a^4D_{5/2} - a^6D_{3/2}$	1.328	10.3 ± 2.0
[Fe II] $a^4D_{5/2} - a^4F_{9/2}$	1.534	19.4 ± 1.5
[Fe II] $a^4D_{3/2} - a^4F_{7/2}$	1.600	11.0 ± 2.1
[Fe II] $a^4D_{7/2} - a^4F_{9/2}$	1.644	133.9 ± 1.5
[Fe II] $a^4D_{5/2} - a^4F_{7/2}$	1.678	12.3 ± 2.4
[Fe II] $a^4D_{3/2} - a^4F_{5/2}$	1.711	5.2 ± 1.8^a
[Fe II] $a^4D_{1/2} - a^4F_{3/2}$	1.745	8.2 ± 1.9
[Fe II] $a^4D_{3/2} - a^4F_{3/2}$	1.798	6.4 ± 2.7^a
[Fe II] $a^4D_{7/2} - a^4F_{7/2} +$ [Fe II] $a^4P_{5/2} - a^4D_{7/2}$	1.810+1.811	36.9 ± 3.8

Notes: ^aS/N between 2 and 3.

The rates of the collisions which excite vibrationally the H_2 molecules (predominantly those with H) increase with the gas density, n_{H} , and the shock velocity, v_s . Hence, departures from LTE tend to decrease with increasing values of n_{H} and v_s . The evolutionary age of the shock wave affects differentially the populations of the more highly excited levels of H_2 . The younger the object, the closer is the shock wave to being pure J-type and the higher are the column densities of the more highly excited rovibrational levels. Furthermore, the populations of these levels tend to be closer to LTE. A higher degree of ionization of the gas (owing to the presence of a background UV radiation field, for example) leads to an increase in the strength of the coupling between the neutral and the charged fluids; this results in a narrower shock wave, nearer to J- than to C-type, and so in this case also the H_2 populations tend to be closer to LTE. In a J-type shock with a magnetic precursor, the levels of $v = 0, 1$ are populated principally in the precursor and exhibit greater departures from LTE than the higher levels. Owing to radiative cascade from excited vibrational states, most of the population remains in the $v = 0$ ground vibrational state. Furthermore, within each vibrational manifold, population tends to accumulate in the lower rotational levels, following rotationally inelastic collisions, mainly with H_2 and He (Flower et al., 2003).

If H_2 is dissociated to H in a J-type shock wave, cooling by atoms and ions, such as C, O, and Fe^+ , can become relatively more important. The emission from (and contribution to the cooling by) these and other important species were computed by the model. In the case of atomic C, we included collisional and radiative transitions between the five energy levels arising from the ^3P , ^1D and ^1S terms using data from the compilation of Mendoza (1983). The model of Fe^+

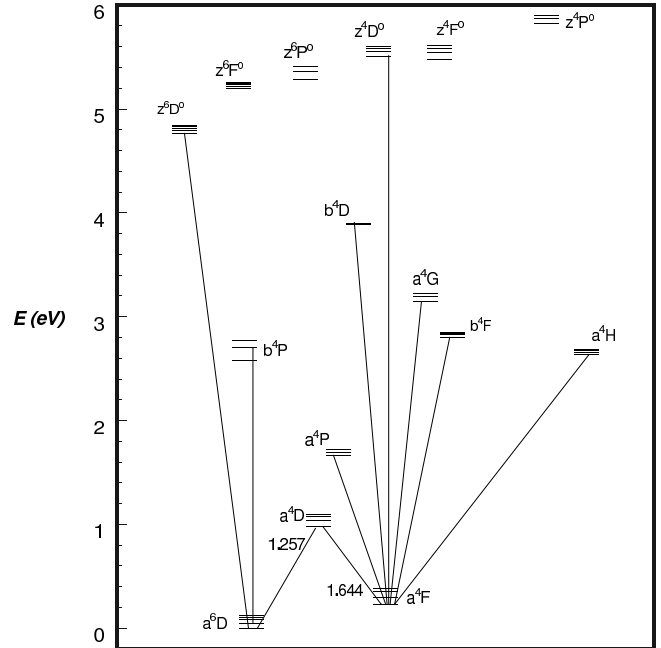


Figure 4. Energy level diagram for Fe^+ . The strongest transition from each of the even parity terms is marked. The odd parity terms decay most strongly to terms with the same multiplicity and the strongest transitions from the z^6D^o and z^4D^o terms are marked as examples. The strongest observed IR transitions, the 1.257 and 1.644 μm lines, are also indicated.

included transitions among the 19 energy levels that arise from the $a^6\text{D}$, $a^4\text{F}$, $a^4\text{D}$, $a^4\text{P}$ and $b^4\text{P}$ terms. The spontaneous radiative transition probabilities computed by Nuss-

baumer & Storey (1988) were used, but, as their data extend only to the a^4P term, the results of Quinet, Le Dourneuf & Zeppen (1996) were adopted for the b^4P term. Giannini et al. (2004) have established that collisions with electrons are likely to dominate the excitation of Fe^+ . The corresponding electron collision strengths were taken from Zhang & Pradhan (1995).

All of the observed [Fe II] IR transitions are from the a^4D term, which lies at an energy of approximately 1 eV (10^4 K) above the ground state: see Figure 4. In order to calculate correctly the populations of the levels of this and other terms, it is necessary to ensure that all significant cascade effects have been included. The highest level of the five terms considered lies at an energy of approximately 3 eV (3×10^4 K), which is lower than the peak temperatures (of order 10^5 K) attained in the J-type shock models. The inclusion of higher energy terms, and in particular the a^4H , b^4F , a^4G and b^4D terms, which decay preferentially to the a^4F term, could conceivably change the distribution of population in the a^4D term. As a check on the convergence of our results, the 50 km s $^{-1}$ J-type shock model considered in Section 3.2 below was rerun, including all of the 142 energy levels for which Zhang & Pradhan (1995) provided data, i.e. levels up to 11.5 eV (1.3×10^5 K) above ground. The set of radiative transition probabilities was extended by means of the data of Quinet et al. (1996), up to the b^4D term, and of Nahar (1995) for the odd parity terms. The overall effect of including these terms is small: the intensities of the [Fe II] lines which are observed were reduced, but by no more than 10%, which is to be compared with the estimated error of 20% in the observed line intensities. We conclude that the basis of 19 levels is sufficient to model the [Fe II] emission lines which are observed, given the current observational uncertainties.

3.1.2 Application

As noted by Davis et al. (1999), and as can be seen in Figure 2, the morphology of the HH99B complex suggests a bow shock. A bow shock can be modelled approximately as a sequence of planar shock fronts, for which the effective shock speed varies with the angle of attack. In the present study, we assume a dissociative J-type shock to occur at the apex of the bow, and J-type shocks with magnetic precursors to dominate in the wings. Each shock model is computed independently of the others, but we consider, in Section 3.2.3, the compatibility of the observations with the sum of the H_2 emission from the different components. We found that a two-component model, comprising a pure J-type shock and a J-type shock with a magnetic precursor, of lower speed, is able to account for the observations of both H_2 and of the atomic and ionic emission lines. More sophisticated treatments of the geometry of bow shocks have been undertaken (e.g. Smith, Brand & Moorhouse, 1990; Smith, Khanzadyan & Davis, 2003). However, it has proved too computationally expensive to include in such models a proper treatment of the chemical and molecular processes that influence shock waves and which are considered here.

The optimal values of the shock speed and pre-shock gas density (in the range $10^3 \leq n_H \leq 10^6$ cm $^{-3}$) were determined by comparing calculated with observed H_2 excitation diagrams and [Fe II] line intensities. The scaling relation

$B(\mu G) = b[n_H(\text{cm}^{-3})]^{0.5}$ determined the initial value of the magnetic induction. Ideally, b should be determined observationally, but this is not generally feasible. In this paper we use the value of $b=1$, consistent with equipartition of energy.

The effect of photoionization processes on the degree of ionization in the gas was simulated by including reactions for species with ionization potentials less than that of H (13.6 eV). For want of more specific information, rates corresponding to the mean interstellar radiation field in the solar neighbourhood (Draine, 1978) were adopted. Photoionization processes are not usually supposed to affect the gas in HH outflows; it is tempting to assume that HH objects are shielded from ionizing photons by the dust in the molecular clouds in which they reside. However, our previous work (Giannini et al., 2004) has shown that the fits to the observed H_2 emission can sometimes be improved by including photoionization by the interstellar background UV radiation field. Accordingly, we investigated systematically whether including photoionization reactions improved the fit of the models to the observations. It was found that including photoionization reactions improved the fits to the observations in all cases.

3.2 Comparison with observations

The present observations of emission lines of H_2 alone are usually insufficient to determine uniquely the shock parameters, notably the shock speed and age and the pre-shock gas density; measurements of the (weaker) lines from levels of still higher excitation, particularly from higher vibrational manifolds, would be required to do so. However, when other observational constraints are taken into account, the range of possible models is more closely circumscribed. First, previous echelle spectroscopy by Davis et al. (1999) provides some constraints on the shock velocity for the knots HH99B1 and HH99B3. Second, it seems reasonable to require that the pre-shock parameters for all the knots which are physically associated should be similar. Third, the models of the H_2 emission should be compatible with the J-type shock models which reproduce the [Fe II] and [C I] emission lines. When these additional factors are taken into account, as described in Sections 3.2.1, 3.2.2 and 3.2.3 below, we find that the models highlighted in Table 3 account best for the H_2 emission observed towards HH99.

3.2.1 H_2 emission

The HH99B bow shock complex is physically connected, and it is reasonable to expect similar pre-shock conditions in all the models of the associated knots. Models with a pre-shock gas density $n_H = 10^4$ cm $^{-3}$, which included photoionization reactions, were found to yield the most consistent fits to the observations of all the HH objects in this complex. The shock velocity was deduced to be about 30 km s $^{-1}$ for all the objects, and the evolutionary ages derived from the models of B0, B2 and B3 were about 120 yr (see Table 3). The observations of B1 from slits 1 and 2 were modelled separately from each other and yielded a similar age (but a greater age than for the other objects). HH99B1 forms part of the head and one wing of the putative bow shock (see Figure 2); it is the only part of the bow shock whose emission

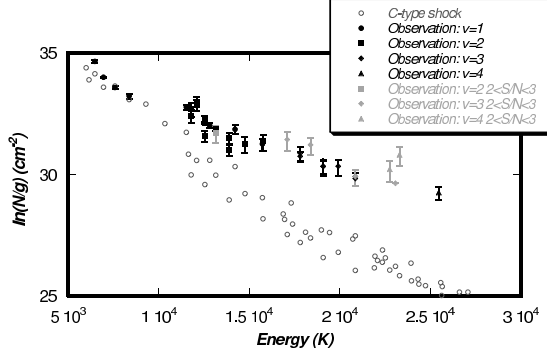


Figure 5. The excitation diagram calculated in a steady-state C-type shock (open circles) underestimates the observed intensities (filled symbols) of high excitation lines.

was measured along the wing (in slit 1), rather than across the head. In addition, the portion of HH99B1 captured in slit 2 lies further back from the apex of the bow shock than any other object (see Figure 2). The degree of excitation of H₂ is expected to decrease along the wing, with increasing distance from the apex, and so it is anticipated (and found) that HH99B1 exhibits a lower degree of excitation than the other associated knots.

The importance of the J-type component of the models, to which we refer as “J-type with magnetic precursor”, may be seen in Fig. (5). There we compare the excitation diagram which derives from the observations of HH99B3 with that calculated in the limit of steady-state, when a pure C-type shock wave obtains. It may be seen that the steady-state structure underestimates the intensities of the H₂ lines of high excitation energy and that the discrepancies increase with the excitation energy. A similar conclusion was reached by Flower et al. (2003) when modelling the outflow Cepheus A West.

A further constraint on v_s in HH99B1 and HH99B3 can be derived from the echelle spectroscopy of Davis et al. (1999). Using the H₂ 2.122 μm line, they measured a FWHM of 15–20 km s^{−1} in B1 and 20–40 km s^{−1} in B3. These observations provide some indication of the flow speed of the neutral gas in the region of the shock in which the lines are excited; but it should be noted that the observed line profiles were not deconvolved from the instrumental profile and that there are (uncertain) line-of-sight projection effects. We note only that the shock velocity of the model for HH99B3 is in good agreement with the measured FWHM, whilst the narrower profile observed in B1 favours the lower velocity model (i.e. $v_s = 30$ km s^{−1}) of the two considered for this knot.

Davis et al. (1999) suggested that HH99A could be either the edge of the HH99B bow shock or a clump of gas which has been overrun by the bow shock. In the latter case, HH99A should have a greater evolutionary age than HH99B. Alternatively, HH99A could be the result of a separate outflow event. Referring to Table 3, we see that all three possible models of HH99A, labelled 1, 2 and 3 in the Table, are more evolved than the corresponding models of HH99B; this is consistent with HH99A being a clump of gas which has been overrun.

The H₂ emission lines observed towards HH99A arise

Table 3. Parameters of possible shock models derived by fitting the H₂ emission from the HH99A and the HH99B complex. Models considered to be the best for each object are in bold face.

Object	v_s	n_H^a	Age
	km s ^{−1}	cm ^{−3}	yr
HH99A(model 1)	50	10 ³	$> 3 \times 10^3$
HH99A(model 2)	34	5×10^3	350
HH99A(model 3)	28	10 ⁴	250
HH99B0	34	10 ⁴	130
HH99B0	18	10 ⁵	40
HH99B1(slit 1)	55	10 ³	400
HH99B1(slit 1)	30	10 ⁴	190
HH99B1(slit 2)	53	10 ³	200
HH99B1(slit 2)	30	10 ⁴	165
HH99B2	55	10 ³	200
HH99B2	33	10 ⁴	125
HH99B3	33	10 ⁴	115

$$^a n_H = n(\text{H}) + 2n(\text{H}_2)$$

from levels with excitation energies up to approximately 2.5×10^4 K. However, observations with S/N > 3 extend only up to 1.5×10^4 K, as compared with $2\text{--}2.5 \times 10^4$ K for the HH99B objects. The lower S/N of the lines of high excitation from HH99A compromises attempts to refine the models further. The excitation diagrams derived from models (open symbols) and observations (corresponding filled symbols) are shown in Figure 6. We plot the results for models 1–3 of HH99A and the models adopted for the HH99B bow shock complex.

From the angular distance between HH99A and the HH99B complex (25'', see Figure 2) and the ages of our shock models, and assuming a distance to HH99 of $d = 130$ pc (Marraco & Rydgren, 1981), a jet speed can be estimated. Taking 120 years as a typical age for the main body of the HH99B complex, and the age of 350 yr from model 2 of HH99A, we find a jet speed of 70 km s^{−1}. This value is similar to the speeds of 80–120 km s^{−1} derived by Davis et al. (1999) from bow shock models (which provided kinematic and spectroscopic data but did not consider the chemistry and atomic processes included in the models presented here) of the HH99 system.

3.2.2 [Fe II] and [C I] emission

The models of HH99 described in Section 3.2.1 above underestimate the observed intensities of the [Fe II] and [C I] lines by several orders of magnitude. Giannini et al. (2004) suggested that the atomic and ionic emission may arise in regions of higher ionization, distinct from those responsible for the H₂ emission: at the apex of a bow shock or in a reverse shock, within the jet, for example. Pure J-type shocks can yield the necessary degrees of ionization, notably of H. The combination of a pure J-type shock and either a pure C-type shock, or a J-type shock with magnetic precursor, may be viewed as an elementary representation of a bow

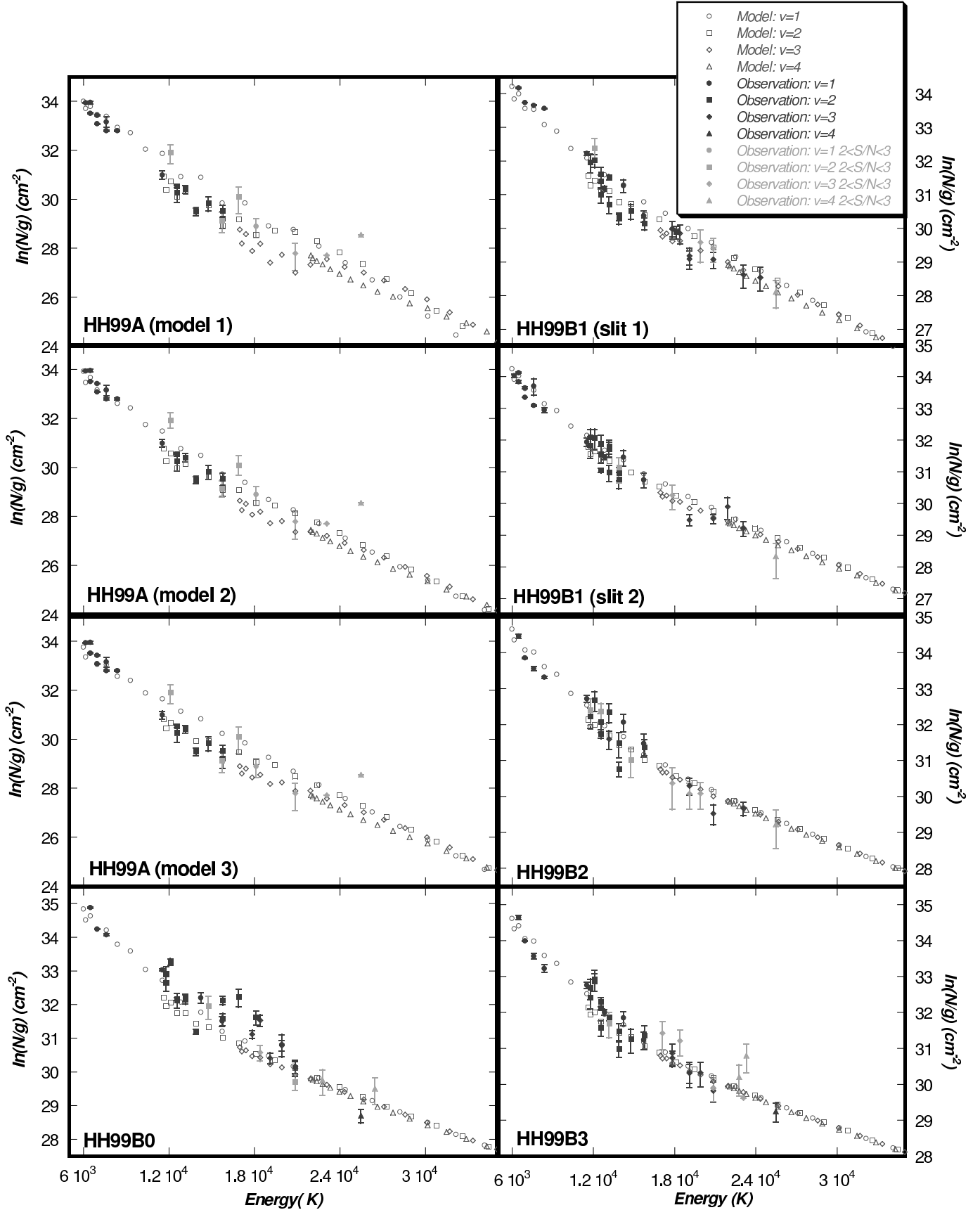


Figure 6. Observed and computed excitation diagrams for HH99. Transitions from the $v = 1$, $v = 2$, $v = 3$ and $v = 4$ vibrational manifolds are denoted by circles, squares, diamonds and triangles, respectively. Open symbols represent the models and filled symbols the observational results, with $S/N > 3$ (black) and $2 < S/N < 3$ (grey).

Table 4. Comparison between observed (reddening corrected, see Table for A_V values) and computed [Fe II] and [C I] line intensities in HH99

Object	Term	$\lambda(\mu\text{m})$	Observed ($I \pm \Delta I$) ($10^{-5} \text{ erg cm}^{-2} \text{ s}^{-1}$)	Model ($10^{-5} \text{ erg cm}^{-2} \text{ s}^{-1}$)
HH99A ¹ $A_V=4.7$	[Fe II] $a^4D_{7/2} - a^6D_{9/2}$	1.257	11.5 ± 0.34	11.5
	[Fe II] $a^4D_{7/2} - a^6D_{7/2}$	1.321	3.83 ± 0.37	3.02
	[Fe II] $a^4D_{7/2} - a^4F_{9/2}$	1.644	8.48 ± 0.31	8.50
	[Fe II] $a^4D_{5/2} - a^4F_{7/2}$	1.677	0.676 ± 0.23	1.59
	[C I] $^1D_2 - ^3P_1$	0.983	10.2 ± 2.0	6.71
	[C I] $^1D_2 - ^3P_2$	0.985	30.1 ± 1.9	19.9
HH99B0 $A_V=4.4$	[Fe II] $a^4D_{7/2} - a^6D_{9/2}$	1.257	40.8 ± 0.34	40.8
	[Fe II] $a^4D_{1/2} - a^6D_{1/2}$	1.271	2.72 ± 0.57	3.45
	[Fe II] $a^4D_{3/2} - a^6D_{3/2}$	1.279	3.49 ± 0.97	5.80
	[Fe II] $a^4D_{5/2} - a^6D_{5/2}$	1.295	5.42 ± 0.59	8.18
	[Fe II] $a^4D_{3/2} - a^6D_{1/2}$	1.298	1.53 ± 0.33	2.54
	[Fe II] $a^4D_{7/2} - a^6D_{7/2}$	1.321	13.0 ± 0.57	10.7
	[Fe II] $a^4D_{5/2} - a^6D_{3/2}$	1.328	3.23 ± 0.63	4.97
	[Fe II] $a^4D_{5/2} - a^4F_{9/2}$	1.534	5.01 ± 0.39	8.68
	[Fe II] $a^4D_{3/2} - a^4F_{7/2}$	1.600	2.70 ± 0.52	6.76
	[Fe II] $a^4D_{7/2} - a^4F_{9/2}$	1.644	31.9 ± 0.36	30.0
	[Fe II] $a^4D_{1/2} - a^4F_{5/2}$	1.664	1.91 ± 0.71^a	3.38
	[Fe II] $a^4D_{5/2} - a^4F_{7/2}$	1.677	2.87 ± 0.56	6.31
	[Fe II] $a^4D_{3/2} - a^4F_{5/2}$	1.711	1.19 ± 0.41^a	1.77
	[Fe II] $a^4D_{1/2} - a^4F_{3/2}$	1.745	1.84 ± 0.43	1.68
	[Fe II] $a^4D_{3/2} - a^4F_{3/2}$	1.798	1.40 ± 0.59^a	3.06
	[C I] $^1D_2 - ^3P_1 + ^1D_2 - ^3P_2$	0.983+0.985	37.2 ± 3.2	40.1
HH99B1 (slit 1) $A_V=6.7$	[Fe II] $a^4D_{7/2} - a^6D_{9/2}$	1.257	9.36 ± 0.35	7.64
	[Fe II] $a^4D_{5/2} - a^4F_{9/2}$	1.534	2.01 ± 0.36	1.66
	[Fe II] $a^4D_{7/2} - a^4F_{9/2}$	1.644	7.06 ± 0.70	5.62
	[C I] $^1D_2 - ^3P_1 + ^1D_2 - ^3P_2$	0.983+0.985	25.3 ± 8.3	61.1
HH99B1 (slit 2) $A_V=6.9$	[Fe II] $a^4D_{7/2} - a^6D_{9/2}$	1.257	35.7 ± 1.7	35.9
	[Fe II] $a^4D_{7/2} - a^6D_{7/2}$	1.321	8.95 ± 0.13	9.41
	[Fe II] $a^4D_{5/2} - a^4F_{9/2}$	1.534	3.13 ± 0.13^a	7.88
	[Fe II] $a^4D_{7/2} - a^4F_{9/2}$	1.644	27.2 ± 0.12	26.4
	[Fe II] $a^4D_{5/2} - a^4F_{7/2}$	1.677	2.84 ± 0.12^a	5.73
	[Fe II] $a^4D_{3/2} - a^4F_{5/2}$	1.711	3.89 ± 0.12	1.61
	[Fe II] $a^4D_{1/2} - a^4F_{3/2}$	1.745	3.90 ± 0.12	1.52
	[C I] $^1D_2 - ^3P_1 + ^1D_2 - ^3P_2$	0.983+0.985	200^b	38.0
HH99B2 $A_V=6.3$	[Fe II] $a^4D_{7/2} - a^6D_{9/2}$	1.257	71.1 ± 1.8	72.7
	[Fe II] $a^4D_{5/2} - a^6D_{5/2}$	1.295	6.18 ± 2.1	14.5
	[Fe II] $a^4D_{7/2} - a^6D_{7/2}$	1.321	21.3 ± 1.8	19.0
	[Fe II] $a^4D_{5/2} - a^6D_{3/2}$	1.328	3.69 ± 1.2	8.84
	[Fe II] $a^4D_{5/2} - a^4F_{9/2}$	1.534	10.3 ± 1.9	15.4
	[Fe II] $a^4D_{3/2} - a^4F_{7/2}$	1.600	4.31 ± 1.5^a	11.9
	[Fe II] $a^4D_{7/2} - a^4F_{9/2}$	1.644	56.1 ± 1.5	53.5
	[Fe II] $a^4D_{1/2} - a^4F_{5/2}$	1.664	6.45 ± 1.6	5.88
	[Fe II] $a^4D_{5/2} - a^4F_{7/2}$	1.677	11.0 ± 3.0	11.2
	[Fe II] $a^4D_{3/2} - a^4F_{5/2}$	1.711	4.96 ± 2.3^a	3.13
	[C I] $^1D_2 - ^3P_1 + ^1D_2 - ^3P_2$	0.983+0.985	94^b	22.5
HH99B3 $A_V=10.3$	[Fe II] $a^4D_{3/2} - a^6D_{5/2}$	1.248	7.31 ± 1.6	0.256
	[Fe II] $a^4D_{7/2} - a^6D_{9/2}$	1.257	45.7 ± 2.0	46.7
	[Fe II] $a^4D_{1/2} - a^6D_{1/2}$	1.271	15.0 ± 2.5	3.93
	[Fe II] $a^4D_{3/2} - a^6D_{3/2}$	1.279	12.2 ± 2.3	6.62
	[Fe II] $a^4D_{7/2} - a^6D_{7/2}$	1.321	24.5 ± 3.1	12.2
	[Fe II] $a^4D_{7/2} - a^4F_{9/2}$	1.644	36.8 ± 0.80	34.4
	[C I] $^1D_2 - ^3P_1 + ^1D_2 - ^3P_2$	0.983+0.985	269^b	36.4

Notes: ¹ Intensities from model (2)^a $2 < S/N < 3$ ^b Upper limit

shock. Accordingly, we have attempted to model the atomic and ionic emission from HH99 with pure J-type shocks. For brevity, we shall refer to the models in the previous Section as ‘H₂ models’ from here on.

Under ‘normal’ interstellar conditions, Fe is strongly depleted from the gas phase, and most of the elemental abundance of Fe (3.23×10^{-5} ; Anders & Grevesse, 1989) is to be found in the grains, probably in the form of silicates. In shock waves, dust grains may be shattered in grain–grain collisions (Jones, Tielens, Hollenbach & McKee, 1994; Jones, Tielens & Hollenbach, 1996; Flower & Pineau des Forêts, 2003). However, this process breaks large grains into smaller grains, rather than releasing elements such as Fe into the gas phase. In a J-type shock wave, the neutral and charged fluids flow with the same speed. On the other hand, the velocity difference between the neutral and charged fluids in C-type shock waves gives rise to collisions between neutrals, such as CO, and charged grains which are sufficiently energetic to result in the erosion of the refractory grain cores (May et al., 2000). Thus, if a C-type shock wave, or a J-type shock with a magnetic precursor, has passed previously through a given region, the fraction of Fe in the gas phase could be significant (providing that there has been insufficient time for grains to reform). In dynamically young objects, such as those under study, which are subject to episodic events on timescales of the order of 500–1000 yr, or even less (e.g. Reipurth & Bally, 2001), we consider that it is reasonable to treat the gas phase abundance of Fe as a variable. Once in the gas phase, Fe is ionized rapidly to Fe⁺ through charge transfer reactions with ions, and the [Fe II] spectrum can be excited, principally by electron collisions, in sufficiently hot gas (Giannini et al., 2004).

We assume that the pure J-type shock propagates into gas with a similar density to that upstream of the corresponding H₂ model. Furthermore, we include photoionization reactions, although these are less significant in the context of the J-type component. J-type shocks which are sufficiently energetic to cause appreciable ionization of H are highly dissociative of H₂ and do not produce significant emission in H₂ over the range of excitation energies covered by the observations. J-type shocks with $v_s \approx 50$ km s^{−1} have peak temperatures of order 10^5 K. The intensities of the [Fe II] lines are insensitive to changes in temperature above 10^4 K, because the levels from which emission arises are close together at 1.1 – 1.3×10^4 K above ground. Consequently, the [Fe II] lines are more sensitive to the abundance of Fe in the gas phase than to the shock velocity, once this is sufficient to give rise to partial ionization of hydrogen. In the models of J-type shocks, $v_s = 50$ km s^{−1} was adopted, together with the pre-shock densities used in the H₂ models, to be found in Table 3. Only the gas phase abundance of Fe differentiated the models: see Table 5.

A comparison of the predicted and observed intensities of both [Fe II] and [C I] lines is presented in Table 4, where only unblended lines of [Fe II] are included. The observations are corrected for reddening, using the power law fit of Cardelli, Clayton & Mathis (1989) to the data of Rieke & Lebofsky (1985), and adopting $R = 3.1$. The predictions of the model are in reasonably good agreement with the observations; the intensities of most of the lines are reproduced to within a factor of 2 (or are consistent with the upper limits for [C I] observed with slit 2). In particular, transitions

Table 5. The percentage of the elemental abundance of Fe in the gas phase, as adopted in the models of pure J-type shocks.

Object	Gas phase Fe
HH99A (model 1)	100
HH99A (model 2)	12
HH99A (model 3)	5
HH99B0	25
HH99B1 (slit 1)	1
HH99B1 (slit 2)	23
HH99B2	71
HH99B3	31

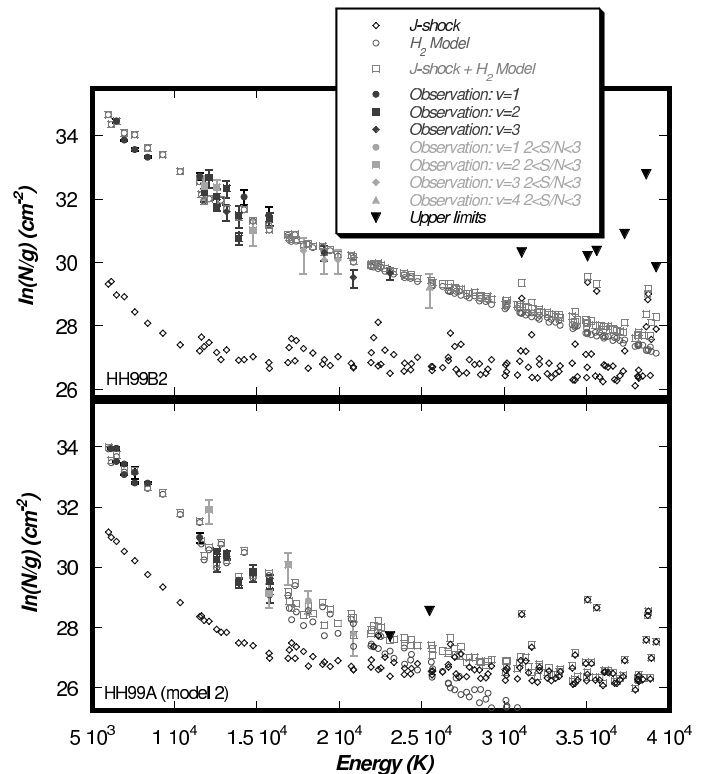


Figure 7. Excitation diagrams from the H₂ models and pure J-type shock components for HH99B2 (upper panel) and model 2 of HH99A (lower panel). The effect of the J-type shock is seen from the sum of the two components, denoted “J-shock + H₂ model”. The contribution to the H₂ emission from the J-type shock is not significant over the range of the observations of HH99B2 but becomes possibly significant for HH99A when the observational upper limits for transitions from levels with excitation energies above 2.2×10^4 K are taken into account.

from the a⁴D_{7/2} term of Fe⁺ are generally reproduced well, especially the strong 1.257 and 1.644 μm lines. On the other hand, the intensity of the 1.248 μm line (from the a⁴D_{3/2} term) observed in HH99B3 is underestimated by more than an order of magnitude. It is possible that this line is partially blended with the nearby 1.247 μm H₂ 2-0 Q(3) line, which is comparable or stronger in intensity. Although these lines show distinct peaks in the spectrum, they are separated by only 9 Å and the de-blending process may not be completely accurate for such a small separation.

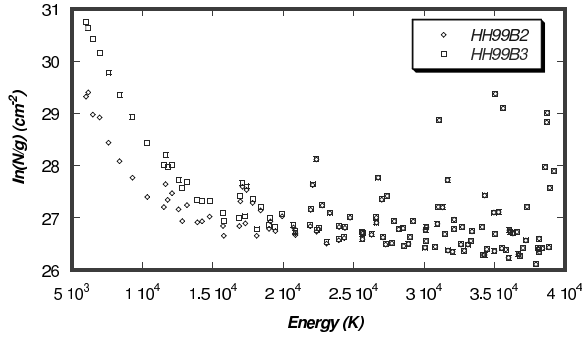


Figure 8. The percentage of Fe in the gas phase is the only parameter which changes between these models of HH99B2 (71%) and HH99B3 (31%). The effect of the different rates of cooling by Fe^+ in the post-shock gas is reflected in the H_2 $v = 1$ level populations.

The intensities of the [C I] lines are reproduced without modification of the pre-shock abundance of C in the gas phase. Approximately 1/3 of the elemental C abundance is already in the gas phase, in the form of CO, which is dissociated at high temperature in reactions with H, producing C and OH. At the peak temperature of these J-type shocks, 99% of the H_2 has been dissociated to H, and nearly all of the CO to C.

3.2.3 H_2 emission from the [Fe II] and [C I] emitting region

In the upper panel of Figure 7, we plot the H_2 excitation diagrams deriving from the J-type shock model and the H_2 model of HH99B2, together with their sum. It can be seen that the contribution to the H_2 emission from the J-type shock is not significant over the observed range of excitation energies; only above 3×10^4 K does the H_2 emission from the J-type shock become important. The shock wave is sufficiently narrow that not all of the excited levels have time to thermalize, and this results in the scatter about the median curve that can be seen in the upper panel of Figure 7. Observational upper limits for HH99B2 are also plotted in the upper panel of Figure 7; they fall well above the model predictions. Similar results were obtained for the other models of HH99B models and are not shown here. The H_2 emission observed towards HH99A exhibits lower excitation than is seen in the bow shock complex. In the case of HH99A, the emission from the J-type shock becomes significant above 2.2×10^4 K (see Figure 7, lower panel). This contribution provides a means of discriminating between the H_2 models of HH99A. When the contribution from the J-type shock is added to that from models 1 and 3 ($n_{\text{H}} = 10^3$ and 10^4 cm^{-3} , respectively), the upper limit to the column density of the $v = 3$ level at 2.3×10^4 K is exceeded. In the case of model 2, this upper limit is not violated.

The rapid and substantial dissociation of H_2 at the peak of these J-type shock models reduces significantly the rate of cooling by H_2 , and atomic/ionic cooling, for example of Fe^+ and O, following electron collisional excitation, can become important. The effect of cooling by Fe^+ is seen in the postshock gas, in the region where the temperature drops

below 10^4 K. At such temperatures, only the $v = 1$ levels of H_2 are significantly populated; the higher vibrational levels are populated immediately behind the shock discontinuity. The effect of the cooling due to Fe^+ , which becomes more pronounced as the gas phase abundance of Fe^+ increases, is to reduce the populations of the H_2 $v = 1$ energy levels. By way of an illustration, we compare, in Figure 8, the excitation diagrams from the J-type shock models of B2 and B3. The only difference between the models is the fraction of Fe in the gas phase (71% for HH99B2 and 31% for HH99B3). It may be seen that the higher gas phase abundance of Fe in the model of HH99B2 results in lower populations of the $v = 1$ energy levels. It should be noted that this effect is not observationally significant: the contribution of the pure J-type shock to the emission from the H_2 $v = 1$ levels is insignificant compared with that of the J-type shock with magnetic precursor.

4 CONCLUSIONS

Spectra in the near IR ($0.98\text{--}2.5 \mu\text{m}$) of HH99 have been presented, which are characterized by prominent emission in both [Fe II] and H_2 transitions. The strongest lines are observed at the head of the bow, where emission in other atomic and ionic lines, of [S II], [N I] and He I, is also observed. The observed intensities of the H_2 , [Fe II] and [C I] emission lines have been used to constrain the parameters of shock models. Our conclusions are as follows:

- with the possible exception of one model of HH99A, all the models which fit the H_2 emission are of J-type shocks with magnetic precursors; this implies that HH99 has not yet reached equilibrium, which is consistent with outflows being young phenomena;
- observations of H_2 lines from higher energy levels are required to constrain further the H_2 models, of HH99A in particular;
- the intensities of the [Fe II] and [C I] emission lines are reproduced satisfactorily by a pure J-type shock with a velocity $v_s = 50 \text{ km s}^{-1}$, which dissociates molecular hydrogen and partially ionizes atomic hydrogen. In particular, the computed intensities of the [Fe II] $1.257 \mu\text{m}$ and $1.644 \mu\text{m}$ lines, the strongest of the observed transitions, are in good agreement with the observations;
- in J-type shocks, Fe^+ becomes a significant coolant in the post-shock gas (owing to dissociation of H_2 to H) and this has consequences for the populations of the $v = 1$ levels of the residual H_2 .

Overall, our results are consistent with the conclusions that outflows are episodic phenomena and that the emission from HH objects arises in bow shocks, with the atomic and ionic emission lines being produced at the apex and the H_2 emission lines in the wings.

Acknowledgments

We thank an anonymous referee for a prompt and helpful report.

REFERENCES

Anders E., Grevesse N. 1989, *Geochim. Cosmochim. Acta*, 53, 197

- Bachiller R. 1996, ARA&A, 34, 111
- Benedettini, M., Giannini, T., Nisini, B. et al. 2000, A&A, 359, 148
- Cardelli J. A., Clayton G. C., Mathis J. S. 1989, ApJ, 345, 245
- Chièze J.-P., Pineau des Forêts G., Flower D.R. 1998, MNRAS, 295, 672
- Cuby J-G., Lidman C., Johnson R., Moutou C. 2003, ISAAC User Manual
- Davis C.J., Smith M.D., Eislöffel J., Davies J.K. 1999, MNRAS, 308, 539
- Davis C.J., Smith M.D., Eislöffel J. 2000, MNRAS, 318, 747
- Draine B. T. 1978, ApJS, 36, 595
- Draine B. T. 1980, ApJ, 241, 1021
- Eislöffel J, Smith M.D, Davis C.J. 2000, A&A, 359, 1147
- Flower D.R., Le Boulrot J., Pineau des Forêts G., Cabrit S. 2003, MNRAS, 341, 70
- Flower D.R., Pineau des Forêts G. 2003, MNRAS, 343, 390
- Giannini T., M^cCoey C., Caratti o Garatti A., Nisini B., Lorenzetti D., Flower D. R. 2004, A&A, in press, astro-ph/0402395
- Gredel R. 1994, A&A, 292, 580
- Gredel R. 1996, A&A, 305, 582
- Hartigan P., Graham J.A. 1987, AJ, 93, 913
- Hartigan P. Curial S, Raymond J, AJ, 347, L31
- Jones A. P., Tielens A. G. G. M, Hollenbach D. J., McKee C. F. 1994, ApJ, 433, 797
- Jones A. P., Tielens A. G. G. M, Hollenbach D. J. 1996, ApJ, 469, 740
- Le Boulrot J., Pineau des Forêts G., Flower D.R., Cabrit S. 2002, MNRAS, 332, 985
- Lesaffre P., Chièze J.-P., Cabrit S., Pineau des Forêts G. I. 2004a, A&A, submitted
- Lesaffre P., Chièze J.-P., Cabrit S., Pineau des Forêts G. II. 2004b, A&A, submitted
- Liseau, R., Ceccarelli, C., Larsson, B. et al. 1996 A&A, 315, L181
- Marraco H. G., Rydgren A. E. 1981, AJ, 86, 62
- May P.W., Pineau des Forêts G., Flower D.R., Field D., Allan N.L., Purton J.A. 2000, MNRAS, 318, 809
- Mendoza C. 1983, in *Planetary Nebulae*, Flower D. R., (ed.), IAU Symp. N. 103, Reidel (Dordrecht), p. 143
- Molinari S., Noriega-Crespo A., Ceccarelli C., Nisini B., Giannini T., Lorenzetti D. et al. 2000, AJ, 538, 698
- Nahar S. N., 1995. A&A, 293, 967
- Nisini B., Caratti o Garatti A., Giannini T., Lorenzetti D. 2002, A&A, 393, 1035
- Nussbaumer H., Storey P. J. 1988, A&A, 193, 327
- Pineau des Forêts G., Flower D.R., Chièze J.-P. 1997, *IAU Symposium no. 182*, ed. Reipurth B., Bertout C., p.199
- Quinet P., Le Dourneuf M., Zeippen C.J. 1996, A&ASS, 120, 361
- Reipurth B., Bally J. 2001, ARA&A, 39, 403
- Rieke G. H., Lebofsky M. J. 1985, ApJ, 288, 618
- Rousselot P., Lidman C., Cuby J-G., Moreels G., Monnet G. 2000, A&A, 354, 1134
- Smith M.D. Brand P.W.J.L., Moorhouse A. 1991, MNRAS, 248, 451
- Smith M.D., Mac Low M.-M. 1997, A&A, 326, 801
- Smith M.D., Khanzadyan T, Davis C.J. 2003, MNRAS, 339, 524
- Van der Blik N.S., Manfroid J., Bouchet P. 1996, A&AS, 119, 547
- Wilking B. A., McCaughrean M. J., Burton M. G., Giblin T., Rayner J. T., Zinnecker H. 1997, AJ, 114, 2029
- Zhang H.L., Pradhan A.K. 1995, A&A, 293, 953

Table 1. Observed lines in HH99 B0. a) H₂ lines.

Term	λ (μm)	$F \pm \Delta$ F ($10^{-16} \text{erg cm}^{-2} \text{s}^{-1}$)
2-0 S(9)	1.053	4.9 ± 2.0^a
2-0 S(7)	1.064	13.4 ± 2.7
2-0 S(6)	1.073	7.4 ± 1.9
2-0 S(5)	1.085	17.6 ± 2.3
2-0 S(4)	1.100	9.1 ± 4.0^a
3-1 S(5)	1.152	6.4 ± 1.3
2-0 S(1)	1.162	5.6 ± 1.2
3-1 S(4)	1.167	3.7 ± 1.2
3-1 S(3)	1.186	5.4 ± 2.0^a
2-0 S(0)	1.189	3.6 ± 1.1
3-1 S(2)	1.207	3.4 ± 1.4^a
4-2 S(6)	1.214	3.2 ± 1.2^a
4-2 S(5)	1.226	3.9 ± 1.2
3-1 S(1)	1.233	5.7 ± 0.7
2-0 Q(1)	1.238	4.6 ± 1.0
2-0 Q(2)+4-2S(4)	1.242+1.242	3.6 ± 0.8
2-0 Q(3)+ [Fe II] $a^4D_{3/2} - a^6D_{5/2}$	1.247+1.248	4.0 ± 1.4^a
2-0 Q(4)	1.254	2.9 ± 0.6
4-2 S(3)+3-1S(0)	1.261+1.262	6.7 ± 1.2
2-0 Q(5)	1.263	5.2 ± 1.7
2-0 Q(7)	1.287	5.2 ± 0.9
4-2 S(1)	1.311	5.0 ± 1.8^a
2-0 O(3)	1.335	5.7 ± 1.3
3-1 Q(5)+4-2S(0)	1.342+1.342	5.9 ± 1.2
1-0 S(9)	1.688	14.2 ± 2.0
1-0 S(8)	1.715	12.1 ± 1.8
1-0 S(7)+ [Fe II] $a^4P_{3/2} - a^4D_{7/2}$	1.748+1.749	47.5 ± 1.4
1-0 S(6)	1.788	34.6 ± 1.3
1-0 S(3)	1.958	199.6 ± 6.5
1-0 S(2)	2.034	61.0 ± 1.8
3-2 S(5)	2.066	7.2 ± 1.4
2-1 S(3)	2.073	18.3 ± 1.4
1-0 S(1)	2.122	147.4 ± 1.4
3-2 S(4)	2.127	4.5 ± 0.7
2-1 S(2)	2.154	13.1 ± 1.4
3-2 S(3)	2.201	8.5 ± 1.4
1-0 S(0)	2.223	48.8 ± 1.1
2-1 S(1)	2.248	26.6 ± 1.2
3-2 S(2)	2.287	7.0 ± 1.2
2-1 S(0)	2.355	14.2 ± 1.3
1-0 Q(1)	2.407	212.4 ± 4.3
1-0 Q(2)	2.413	84.7 ± 4.3
1-0 Q(3)	2.424	209.5 ± 4.3
1-0 Q(4)	2.437	67.1 ± 4.1
1-0 Q(5)	2.455	54.5 ± 4.9
1-0 Q(6)	2.476	48.9 ± 11.7
1-0 Q(7)	2.500	140.8 ± 15.0

Notes: ^aS/N between 2 and 3.

Table 1. Observed lines in HH99 B0. b) Atomic and Ionic lines.

Term	λ (μm)	$F \pm \Delta F$ ($10^{-16} \text{erg cm}^{-2} \text{s}^{-1}$)
[C I] $^1D_2 - ^3P_1 +$ [C I] $^1D_2 - ^3P_2$	0.983+0.985	66.1 ± 5.6
[S II] $^2P_{3/2} - ^2D_{3/2}$	1.029	10.3 ± 1.7
[S II] $^2P_{3/2} - ^2D_{5/2}$	1.032	9.5 ± 1.2
[S II] $^2P_{3/2} - ^2D_{3/2}$	1.034	5.6 ± 1.0
[N I] $^2P_{3/2,1/2} - ^2D_{5/2} + ^2P_{3/2,1/2} - ^2D_{3/2}$	1.040+1.041	11.4 ± 2.2
He I $^3S_1 - ^3P_{0,1,2}^o$	1.083	7.9 ± 2.1
[Fe II] $a^4D_{7/2} - a^6D_{9/2}$	1.257	119.1 ± 1.0
[Fe II] $a^4D_{1/2} - a^6D_{1/2}$	1.271	8.1 ± 1.7
[Fe II] $a^4D_{3/2} - a^6D_{3/2}$	1.279	10.5 ± 2.9
Pa β	1.282	4.8 ± 2.0^a
[Fe II] $a^4D_{5/2} - a^6D_{5/2}$	1.295	16.6 ± 1.8
[Fe II] $a^4D_{3/2} - a^6D_{1/2}$	1.298	4.7 ± 1.0
[Fe II] $a^4D_{7/2} - a^6D_{7/2}$	1.321	41.0 ± 1.8
[Fe II] $a^4D_{5/2} - a^6D_{3/2}$	1.328	10.3 ± 2.0
[Fe II] $a^4D_{5/2} - a^4F_{9/2}$	1.534	19.4 ± 1.5
[Fe II] $a^4D_{3/2} - a^4F_{7/2}$	1.600	11.0 ± 2.1
[Fe II] $a^4D_{7/2} - a^4F_{9/2}$	1.644	133.9 ± 1.5
[Fe II] $a^4D_{5/2} - a^4F_{7/2}$	1.678	12.3 ± 2.4
[Fe II] $a^4D_{3/2} - a^4F_{5/2}$	1.711	5.2 ± 1.8^a
[Fe II] $a^4D_{1/2} - a^4F_{3/2}$	1.745	8.2 ± 1.9
[Fe II] $a^4D_{3/2} - a^4F_{3/2}$	1.798	6.4 ± 2.7^a
[Fe II] $a^4D_{7/2} - a^4F_{7/2} +$ [Fe II] $a^4P_{5/2} - a^4D_{7/2}$	1.810+1.811	36.9 ± 3.8

Notes: ^aS/N between 2 and 3.

Table 2. Observed lines in HH99 B1 slit1. a) H₂ lines.

Term	λ (μm)	$F \pm \Delta F$ ($10^{-16} \text{erg cm}^{-2} \text{s}^{-1}$)
2-0 S(7)	1.064	12.2 ± 2.2
2-0 S(5)	1.085	12.1 ± 2.1
3-1 S(8)	1.124	2.8 ± 0.9
2-0 S(2)	1.130	8.5 ± 2.8
3-1 S(7)	1.138	6.4 ± 1.9
3-1 S(5)	1.152	10.7 ± 2.5
2-0 S(1)	1.162	15.4 ± 3.5
3-1 S(3)	1.186	7.8 ± 2.0
2-0 S(0)	1.189	5.1 ± 1.8^a
3-1 S(2)	1.207	3.7 ± 1.0
4-2 S(5)	1.226	4.4 ± 1.7^a
3-1 S(1)	1.233	7.9 ± 2.0
2-0 Q(1)	1.238	10.2 ± 2.8
2-0 Q(2)+4-2S(4)	1.242+1.242	5.6 ± 1.6
2-0 Q(3)	1.247	9.0 ± 1.8
2-0 Q(4)	1.254	2.9 ± 0.7
4-2 S(3)+3-1S(0)	1.261+1.262	5.2 ± 0.9
2-0 Q(5)	1.263	4.6 ± 0.8
3-1 Q(5)+4-2S(0)	1.342+1.342	7.4 ± 0.6
3-1 Q(7)	1.368	6.6 ± 2.4^a
1-0 S(9)	1.688	15.9 ± 2.6
1-0 S(8)	1.715	16.6 ± 3.1
1-0 S(7)	1.748	52.2 ± 4.0
1-0 S(6)	1.788	52.4 ± 2.5
1-0 S(3)	1.958	456.5 ± 7.1
2-1 S(4)	2.004	11.3 ± 2.5
1-0 S(2)	2.034	128.3 ± 1.9
2-1 S(3)	2.073	24.6 ± 2.4
1-0 S(1)	2.122	280.5 ± 1.6
3-2 S(4)	2.127	4.2 ± 1.9^a
2-1 S(2)	2.154	21.1 ± 1.5
3-2 S(3)	2.201	7.0 ± 1.8
1-0 S(0)	2.223	74.2 ± 1.5
2-1 S(1)	2.248	25.8 ± 5.8
2-1 S(0)	2.355	12.3 ± 2.4
3-2 S(1)	2.386	9.7 ± 2.2
1-0 Q(1)	2.407	287.4 ± 10.0
1-0 Q(2)	2.413	125.0 ± 10.2
1-0 Q(3)	2.424	246.9 ± 9.4
1-0 Q(4)	2.437	94.8 ± 10.2
1-0 Q(5)	2.455	58.5 ± 9.9
1-0 Q(6)	2.476	71.7 ± 8.9
1-0 Q(7)	2.500	212.5 ± 28.6

Notes: ^aS/N between 2 and 3.**Table 2.** Observed lines in HH99 B1 slit1. b) Atomic and Ionic lines.

Term	λ (μm)	$F \pm \Delta F$ ($10^{-16} \text{erg cm}^{-2} \text{s}^{-1}$)
[C I] $^1D_2 - ^3P_1 +$ [C I] $^1D_2 - ^3P_2$	0.983+0.985	30.6 ± 10.0
[Fe II] $a^4D_{7/2} - a^6D_{9/2}$	1.257	27.0 ± 1.0
[Fe II] $a^4D_{5/2} - a^4F_{9/2}$	1.534	9.5 ± 1.7
[Fe II] $a^4D_{7/2} - a^4F_{9/2}$	1.644	38.3 ± 3.8

Notes: ^aS/N between 2 and 3.

Table 3. Observed lines in HH99 B1 slit2. a) H₂ lines.

Term	λ (μm)	$F \pm \Delta F$ ($10^{-16} \text{erg cm}^{-2} \text{s}^{-1}$)
2-0 S(3)	1.117	8.9 ± 1.9
3-1 S(9)+3-1S(10)+3-1S(11)	1.120+1.120+1.121	8.5 ± 2.2
3-1 S(8)	1.124	5.5 ± 1.7
3-1 S(7)	1.130	7.9 ± 1.8
2-0 S(2)	1.138	4.7 ± 1.1
3-1 S(6)	1.140	6.1 ± 1.2
3-1 S(5)	1.152	8.6 ± 1.3
2-0 S(1)	1.162	7.7 ± 2.0
3-1 S(3)	1.186	5.4 ± 0.9
2-0 S(0)	1.189	5.1 ± 1.7
4-2 S(5)	1.226	3.6 ± 1.2
3-1 S(1)	1.233	3.7 ± 1.4^a
2-0 Q(1)	1.238	6.1 ± 1.6
2-0 Q(3)	1.247	5.3 ± 1.4
2-0 Q(4)	1.254	2.9 ± 0.6
4-2 S(3)+3-1S(0)	1.261+1.262	4.8 ± 1.3
2-0 Q(5)	1.263	3.3 ± 1.2^a
2-0 O(3)	1.335	4.1 ± 1.4
3-1 Q(5)+4-2S(0)	1.342+1.342	4.7 ± 1.4
1-0 S(9)	1.688	13.1 ± 2.3
1-0 S(8)	1.715	12.1 ± 3.0
1-0 S(7)	1.748	36.7 ± 2.7
1-0 S(6)	1.788	21.0 ± 2.6
1-0 S(3)	1.958	119.0 ± 1.7
1-0 S(2)	2.034	39.1 ± 0.9
2-1 S(3)	2.073	9.5 ± 1.6
1-0 S(1)	2.122	102.0 ± 0.7
2-1 S(2)	2.154	4.3 ± 0.6
1-0 S(0)	2.223	28.5 ± 1.2
2-1 S(1)	2.248	14.4 ± 1.0
2-1 S(0)	2.355	8.1 ± 2.1
1-0 Q(1)	2.407	114.0 ± 3.4
1-0 Q(2)	2.413	48.8 ± 3.9
1-0 Q(3)	2.424	106.0 ± 4.1
1-0 Q(4)	2.437	61.0 ± 5.7
1-0 Q(5)	2.455	26.2 ± 4.9

Notes: ^aS/N between 2 and 3.**Table 3.** Observed lines in HH99 B1 slit2. b) Atomic and Ionic lines.

Term	λ (μm)	$F \pm \Delta F$ ($10^{-16} \text{erg cm}^{-2} \text{s}^{-1}$)
[Fe II] $a^4D_{3/2} - a^6D_{5/2}$	1.248	4.4 ± 1.6^a
[Fe II] $a^4D_{7/2} - a^6D_{9/2}$	1.257	34.0 ± 1.6
[Fe II] $a^4D_{7/2} - a^6D_{7/2}$	1.321	9.8 ± 1.4
[Fe II] $a^4D_{5/2} - a^4F_{9/2}$	1.534	4.9 ± 2.1^a
[Fe II] $a^4D_{7/2} - a^4F_{9/2}$	1.644	48.9 ± 2.2
[Fe II] $a^4D_{5/2} - a^4F_{7/2}$	1.678	5.3 ± 2.3^a
[Fe II] $a^4D_{3/2} - a^4F_{5/2}$	1.711	7.5 ± 2.4
[Fe II] $a^4D_{1/2} - a^4F_{3/2}$	1.745	7.8 ± 2.3
[Fe II] $a^4D_{7/2} - a^4F_{7/2} + [\text{Fe II}] a^4P_{5/2} - a^4D_{7/2}$	1.810+1.811	10.2 ± 2.4

Notes: ^aS/N between 2 and 3.

Table 4. Observed lines in HH99 B2. a) H₂ lines.

Term	λ (μm)	$F \pm \Delta F$ ($10^{-16}\text{erg cm}^{-2}\text{s}^{-1}$)
2-0 S(3)	1.117	2.8 ± 0.8
3-1 S(9)+3-1S(10)+3-1S(11)	1.120+1.120+1.121	2.6 ± 0.8
3-1 S(7)	1.130	4.6 ± 0.9
2-0 S(2)	1.138	3.2 ± 0.8
3-1 S(5)	1.152	3.2 ± 0.9
2-0 S(1)	1.162	4.7 ± 1.2
3-1 S(3)	1.186	4.6 ± 1.1
4-2 S(5)	1.226	2.0 ± 0.9^a
3-1 S(1)	1.233	2.3 ± 1.1^a
2-0 Q(1)	1.238	3.1 ± 1.1^a
2-0 Q(3)	1.247	4.6 ± 1.1
4-2 S(3)+3-1S(0)	1.261+1.262	2.7 ± 0.8
2-0 Q(7)	1.287	3.5 ± 0.7
2-0 O(3)	1.335	2.3 ± 0.6
1-0 S(9)	1.688	9.4 ± 3.0
1-0 S(8)	1.715	7.3 ± 1.7
1-0 S(7)+ [Fe II] $a^4P_{3/2} - a^4D_{7/2}$	1.748+1.749	22.4 ± 1.9
1-0 S(6)	1.788	17.1 ± 1.7
1-0 S(3)	1.958	68.0 ± 1.1
2-1 S(4)	2.004	3.7 ± 1.4^a
1-0 S(2)	2.034	23.3 ± 1.2
2-1 S(3)	2.073	6.2 ± 1.2
1-0 S(1)	2.122	63.4 ± 1.1
3-2 S(4)	2.127	1.4 ± 0.5^a
2-1 S(2)	2.154	4.6 ± 1.1
3-2 S(3)	2.201	3.7 ± 1.3^a
1-0 S(0)	2.223	20.0 ± 1.1
2-1 S(1)	2.248	10.8 ± 1.2
2-1 S(0)	2.355	4.8 ± 1.3
1-0 Q(1)	2.407	105.0 ± 3.6
1-0 Q(2)	2.413	43.6 ± 3.5
1-0 Q(3)	2.424	106.0 ± 3.5
1-0 Q(4)	2.437	45.6 ± 4.0
1-0 Q(5)	2.455	19.9 ± 3.4
1-0 Q(6)	2.476	37.5 ± 16.8

Notes: ^aS/N between 2 and 3.**Table 4.** Observed lines in HH99 B2. b) Atomic and Ionic lines.

Term	λ (μm)	$F \pm \Delta F$ ($10^{-16}\text{erg cm}^{-2}\text{s}^{-1}$)
[Fe II] $a^4D_{7/2} - a^6D_{9/2}$	1.257	32.1 ± 0.8
[Fe II] $a^4D_{5/2} - a^6D_{5/2}$	1.295	3.0 ± 1.0
[Fe II] $a^4D_{7/2} - a^6D_{7/2}$	1.321	10.8 ± 0.9
[Fe II] $a^4D_{5/2} - a^6D_{3/2}$	1.328	1.9 ± 0.6
[Fe II] $a^4D_{5/2} - a^4F_{9/2}$	1.534	7.1 ± 1.3
[Fe II] $a^4D_{3/2} - a^4F_{7/2}$	1.600	3.2 ± 1.1^a
[Fe II] $a^4D_{7/2} - a^4F_{9/2}$	1.644	43.5 ± 1.2
[Fe II] $a^4D_{1/2} - a^4F_{5/2}$	1.664	5.1 ± 1.3
[Fe II] $a^4D_{5/2} - a^4F_{7/2}$	1.678	8.8 ± 2.4
[Fe II] $a^4D_{3/2} - a^4F_{5/2}$	1.711	4.1 ± 1.9^a
[Fe II] $a^4D_{7/2} - a^4F_{7/2} + [\text{Fe II}] a^4P_{5/2} - a^4D_{7/2}$	1.810+1.811	36.9 ± 3.8

Notes: ^aS/N between 2 and 3.

Table 5. Observed lines in HH99 B3. a) H₂ lines.

Term	λ (μm)	$F \pm \Delta F$ ($10^{-16}\text{erg cm}^{-2}\text{s}^{-1}$)
3-1 S(5)	1.152	7.2 ± 2.0
2-0 S(1)	1.162	10.0 ± 1.2
3-1 S(4)	1.169	3.9 ± 1.2
3-1 S(3)	1.186	3.9 ± 0.9
2-0 S(0)	1.189	2.8 ± 0.8
4-2 S(5)	1.226	4.6 ± 1.2
3-1 S(1)	1.233	5.5 ± 1.2
2-0 Q(1)	1.238	6.8 ± 1.9
2-0 Q(3)	1.247	3.5 ± 0.7
2-0 Q(4)	1.254	1.7 ± 0.6^a
4-2 S(3)+3-1S(0)	1.261+1.262	4.8 ± 1.0
2-0 Q(5)	1.263	4.8 ± 1.1
4-2 S(2)	1.285	3.4 ± 1.6^a
2-0 Q(7)	1.287	5.7 ± 1.8
4-2 S(1)	1.311	5.6 ± 2.3^a
3-1 Q(1)	1.314	5.3 ± 2.0^a
2-0 O(3)	1.335	4.6 ± 1.3
3-1 Q(5)+4-2S(0)	1.342+1.342	3.8 ± 1.2
1-0 S(9)	1.688	12.5 ± 3.0
1-0 S(8)	1.715	9.7 ± 1.8
1-0 S(7)+ [Fe II] $a^4P_{3/2} - a^4D_{7/2}$	1.748+1.749	39.5 ± 3.4
1-0 S(6)	1.788	29.7 ± 2.7
1-0 S(3)	1.958	103.0 ± 6.1
2-1 S(4)	2.004	4.1 ± 1.3
1-0 S(2)	2.034	37.7 ± 1.8
3-2 S(5)	2.065	5.9 ± 2.2^a
2-1 S(3)	2.073	13.1 ± 1.6
1-0 S(1)	2.122	120.0 ± 1.1
2-1 S(2)	2.154	9.8 ± 0.8
3-2 S(3)	2.201	8.0 ± 2.6
1-0 S(0)	2.223	39.9 ± 1.5
2-1 S(1)	2.248	26.4 ± 1.2
3-2 S(2)	2.287	5.2 ± 1.8^a
2-1 S(0)	2.355	13.0 ± 2.3
3-2 S(1)	2.386	9.7 ± 1.9
1-0 Q(1)	2.407	223.3 ± 3.6
1-0 Q(2)	2.413	93.1 ± 3.8
1-0 Q(3)	2.424	221.1 ± 3.4
1-0 Q(4)	2.437	89.3 ± 3.6
1-0 Q(5)	2.455	36.8 ± 3.4
1-0 Q(6)	2.476	111.2 ± 9.0

Notes: ^aS/N between 2 and 3.**Table 5.** Observed lines in HH99 B3. b) Atomic and Ionic lines.

Term	λ (μm)	$F \pm \Delta F$ ($10^{-16}\text{erg cm}^{-2}\text{s}^{-1}$)
[Fe II] $a^4D_{3/2} - a^6D_{5/2}$	1.248	3.2 ± 0.7
[Fe II] $a^4D_{7/2} - a^6D_{9/2}$	1.257	20.6 ± 0.9
[Fe II] $a^4D_{1/2} - a^6D_{1/2}$	1.271	7.1 ± 1.2
[Fe II] $a^4D_{3/2} - a^6D_{3/2}$	1.279	5.9 ± 1.1
[Fe II] $a^4D_{7/2} - a^6D_{7/2}$	1.321	13.5 ± 1.7
[Fe II] $a^4D_{7/2} - a^4F_{9/2}$	1.644	41.0 ± 0.5

Notes: ^aS/N between 2 and 3.

Table 6. Observed lines in HH99 A. a) H₂ lines.

Term	λ (μm)	$F \pm \Delta F$ ($10^{-16}\text{erg cm}^{-2}\text{s}^{-1}$)
2-0 S(7)	1.064	8.1 ± 2.9^a
2-0 S(6)	1.073	8.0 ± 4.0^a
2-0 S(5)	1.085	8.5 ± 2.8
3-1 S(5)	1.152	3.6 ± 1.6^a
2-0 S(1)	1.162	6.6 ± 2.2
2-0 Q(7)	1.287	4.3 ± 1.1
1-0 S(9)	1.688	5.7 ± 2.2^a
1-0 S(7)+ [Fe II] $a^4P_{3/2} - a^4D_{7/2}$	1.748+1.749	27.6 ± 2.6
1-0 S(6)	1.788	18.4 ± 2.8
1-0 S(3)	1.958	246.0 ± 8.7
2-1 S(4)	2.004	6.6 ± 1.8
1-0 S(2)	2.034	62.2 ± 2.2
2-1 S(3)	2.073	12.0 ± 1.8
1-0 S(1)	2.122	163.2 ± 2.4
2-1 S(2)	2.154	7.8 ± 1.2
1-0 S(0)	2.223	42.3 ± 1.1
2-1 S(1)	2.248	17.7 ± 1.3
2-1 S(0)	2.355	12.0 ± 4.4^a
1-0 Q(1)	2.407	187.1 ± 3.8
1-0 Q(2)	2.413	75.4 ± 4.1
1-0 Q(3)	2.424	169.0 ± 4.6
1-0 Q(4)	2.437	52.3 ± 10.7

Notes: ^aS/N between 2 and 3.**Table 6.** Observed lines in HH99 A. b) Atomic and Ionic lines.

Term	λ (μm)	$F \pm \Delta F$ ($10^{-16}\text{erg cm}^{-2}\text{s}^{-1}$)
[C I] $^1D_2 - ^3P_1$	0.983	23.9 ± 4.6
[C I] $^1D_2 - ^3P_2$	0.985	71.4 ± 4.6
[S II] $^2P_{3/2} - ^2D_{3/2}$	1.029	7.4 ± 1.5
[S II] $^2P_{3/2} - ^2D_{5/2}$	1.032	4.6 ± 1.3
[Fe II] $a^4D_{7/2} - a^6D_{9/2}$	1.257	50.4 ± 1.5
[Fe II] $a^4D_{7/2} - a^6D_{7/2}$	1.321	18.6 ± 1.8
[Fe II] $a^4D_{7/2} - a^4F_{9/2}$	1.644	58.6 ± 2.2
[Fe II] $a^4D_{5/2} - a^4F_{7/2}$	1.678	4.8 ± 1.6
[Fe II] $a^4D_{7/2} - a^4F_{7/2}$ + [Fe II] $a^4P_{5/2} - a^4D_{7/2}$	1.810+1.811	20.1 ± 6.5

Notes: ^aS/N between 2 and 3.